entropy

MDPI

Article

Lattice Distortions in the FeCoNiCrMn High Entropy Alloy Studied by Theory and Experiment

Hyun Seok Oh [1,2], Duancheng Ma [2,†], Gerard Paul Leyson [2], Blazej Grabowski [2], Eun Soo Park [1,*], Fritz Körmann [3,*] and Dierk Raabe [2]

1 Department of Materials Science and Engineering, Seoul National University, Seoul 151-744, Korea; hyunseok07@snu.ac.kr

2 Max-Planck-Institut für Eisenforschung GmbH, 40237 Düsseldorf, Germany; d.ma@mpie.de (D.M.); leyson@mpie.de (G.P.L.); grabowski@mpie.de (B.G.); raabe@mpie.de (D.R.)

3 Department of Materials Science and Engineering, Delft University of Technology, Mekelweg 2, 2628 CD Delft, The Netherlands

* Correspondence: espark@snu.ac.kr (E.S.P.); f.h.w.kormann@tudelft.nl (F.K.); Tel.: +82-2-880-7221 (E.S.P.); +31-15-278-1972 (F.K.)

† Current address: LKR Leichtmetallkompetenzzentrum Ranshofen GmbH, Lamprechtshausenerstr. 61, 5282 Ranshofen-Braunau, Austria.

Academic Editor: An-Chou Yeh

Received: 8 July 2016; Accepted: 29 August 2016; Published: 2 September 2016

Abstract: Lattice distortions constitute one of the main features characterizing high entropy alloys. Local lattice distortions have, however, only rarely been investigated in these multi-component alloys. We, therefore, employ a combined theoretical electronic structure and experimental approach to study the atomistic distortions in the FeCoNiCrMn high entropy (Cantor) alloy by means of density-functional theory and extended X-ray absorption fine structure spectroscopy. Particular attention is paid to element-resolved distortions for each constituent. The individual mean distortions are small on average, <1%, but their fluctuations (i.e., standard deviations) are an order of magnitude larger, in particular for Cr and Mn. Good agreement between theory and experiment is found.

Keywords: high entropy alloy; lattice distortions; density functional theory; extended X-ray absorption fine-structure spectroscopy

1. Introduction

High configurational entropy, sluggish diffusion, the cocktail effect and lattice distortions constitute the four main features, also referred to as core effects, characterizing the broad class of multi-principal element solid solution alloys known as high entropy alloys (HEAs) [1–3]. The term cocktail effect refers to the fact that some properties (e.g., mechanical or magnetic ones) cannot be approximated from linear interactions among the different elements and phases. This class of alloys has attracted a lot of attention due to promising mechanical [4–8], electric [9,10] and magnetic properties [11,12]. The core effects have originally been assumed to be responsible for the excellent properties of HEAs. Recently, it was shown, however, that the efficiency and relevance of the core effects need to be critically examined for each specific system under consideration. For example, in the FeCoNiCrMn alloy, other entropy contributions, i.e., lattice vibrations, electrons and magnetism, were shown to be of similar importance as the configurational entropy [13].

In the present study, we focus on lattice distortions that control the solid solution strengthening in metals. Due to random fluctuations, these lattice distortions can introduce energy barriers against dislocation motion. This strengthening mechanism was originally introduced by Labusch [14,15] and recently extended to HEAs by Varvenne et al. [16]. The key parameter that controls this strengthening mechanism is the solute-dislocation interaction energy.

For fcc materials, solutes can be approximated as point dilatational sources. In this case, the interaction energy between a dislocation at the origin and a solute at position $\vec{r}$ is:

$$U(\vec{r}) = -p(\vec{r})\,\Delta V_m, \tag{1}$$

where $p(\vec{r})$ is the dislocation pressure field and ΔV_m is the misfit volume of the solute, which is defined here as the difference between the volume of the solute in the alloy and the average atomic volume [17]. For dilute alloys, the average atomic volume can be well approximated by the volume of the host matrix, which means that the matrix atoms essentially have zero misfit in the alloy. In HEAs, however, the average effective medium does not correspond to any specific constituent element. The atoms in an HEA can, therefore, be seen as "solutes" with respect to the effective medium (i.e., each atom has a misfit volume) [16]. Further, the misfit volume of an element in this class of materials is not only dependent on the element itself, but also on the local chemical environment in which the element is embedded. The misfit volume of element i can be expressed as,

$$\Delta V_m^i(\vec{r}) = \overline{\Delta V}_m^i + \delta V_m^i(\vec{r}), \tag{2}$$

where $\overline{\Delta V}_m^i$ is the mean misfit volume of element i and $\delta V_m^i(\vec{r})$ is the fluctuation of the misfit volume due to the local chemical environment, which will have a characteristic distribution for a given alloy. Solute strengthening arises from fluctuations in the solute-dislocation interaction energy [14,15]. In dilute alloys, these fluctuations originate from spatial fluctuations in the solute concentration. In HEAs, however, there is an additional contribution due to the fluctuations in the misfit volumes themselves. In order to understand solute strengthening in HEAs, it is important to understand not only the average misfit $\overline{\Delta V_m^i}$, but also its distribution around the mean.

Wang [18] employed empirical pair-potentials to study lattice distortions in fcc and bcc HEAs. However, empirical pair-potentials do not take the underlying electronic structure and magnetic effects into account, both of which may cause additional distortion effects. Density-functional-theory (DFT) calculations for FeCoNiCr and FeCoNi revealed that electronic charge transfer causes a local atomic pressure on the individual constituents, which could result in local volume fluctuations [19]. Further DFT studies revealed strong element-specific magnetic moment fluctuations in fcc FeCoNiCr, which are ultimately rooted in local electronic structure effects [20–22]. In particular anti-ferromagnetic Cr plays a crucial role [20]. By mixing ferro- and anti-ferromagnetic elements, significant element-specific local lattice fluctuations can be expected. At the same time, a small amount of local distortions is intrinsically assumed in many recent DFT studies relying on perfect (distortion free) crystal structures by employing the coherent potential approximation [11,13,23–26]. A pragmatic reason behind this assumption is the significantly larger computational demands of alternative supercell approaches.

Experimental studies identifying the role of local distortions are mostly carried out by standard X-ray or neutron diffraction techniques, providing, however, only information on lattice distortions averaged over all elements [27,28]. An alternative is given by the more recent technique of extended X-ray absorption fine structure (EXAFS) giving access to element-specific mean distortions. Local fluctuations (standard deviations) due to the chemical environment are very difficult to experimentally extract due to additional thermal fluctuations [27]. The latter can be "switched off" in electronic structure calculations, such as DFT. The same holds true for the impact of magnetism, which can be estimated in DFT simulations by performing non-spin polarized calculations.

In this work we, therefore, conducted a combined experimental (EXAFS) and theoretical (DFT) study to investigate element resolved local-distortions and their impact on magnetism and the relation to solid solution strengthening. As an application, we have chosen the well-studied prototype equi-atomic fcc FeCoNiCrMn HEA, also known as Cantor alloy. We discuss not only the mean distortions, but also the element resolved distortion fluctuations, which are, as mentioned above, a critical input to state-of-the-art solid-solution strengthening models.

2. Materials and Methods

The FeCoNiCrMn HEA was cast in a vacuum induction furnace using metallurgical ingredients above 99.8 wt % purity. To remove artifacts, such as pores or elemental segregation, as well as to enhance the overall quality of the homogenized sample, the as-cast ingot was hot rolled at 900 °C with a rolling reduction ratio of 50%, followed by homogenization at 1200 °C for 3 h in an Ar atmosphere and eventually quenched in water. The bulk sample was mechanically ground into a 15 µm-thick ribbon, with SiC abrasive paper down to P4000. Chemical analysis revealed a nearly equi-atomic composition of Fe 20.4−Co 20.1−Ni 20.1−Cr 19.7−Mn 19.7 at %.

Recent findings showed phase decomposition in the FeCoNiCrMn alloy [29], and we, therefore, probed the compositional homogeneity at the atomic scale using atom probe tomography (LEAP 5000 XS, Cameca Inc., Düsseldorf, Germany) to verify a single-phase solid solution in the present samples. The results shown in Figure 1 reveal no indication of any compositional decomposition on the nm-scale. The normalized homogenization parameter μ obtained by a frequency distribution analysis is close to 0 for all five elements (not shown), revealing a random distribution of the involved elements in the present alloy. This is a direct consequence of our sample preparation and the sufficiently high enough temperatures chosen for homogenization.

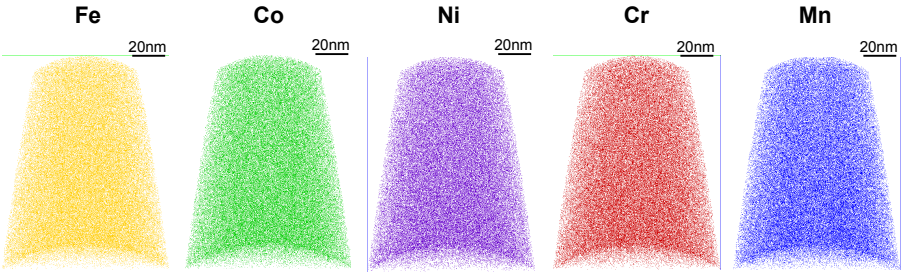

Figure 1. Atom probe tomography results for the investigated samples.

X-ray absorption measurements were carried out on the 7D beamline of the Pohang Accelerator Laboratory (PLS-II, 3.0 GeV, Pohang, Korea). The X-ray absorption spectra for Cr, Mn, Fe, Co and Ni were taken in a transmission mode under a He atmosphere. Higher-order harmonic rejection was achieved by detuning the Si(111) monochromator crystals to 15%–30% for each element edge. The beam size was 1.5 × 4 mm in the horizontal and vertical directions to include more than 100 grains for uniformity. The X-ray absorption spectra for Cr, Mn, Fe, Co and Ni were taken in a transmission mode under ambient conditions. All element foils were measured as a reference to calibrate for any inconsistency in the energy shifts during the data collection. The obtained datasets were properly aligned and processed using the program Athena in the IFEFFIT 1.2.11d suite of software programs [30]. The smooth pre-edge function has been removed by linear extrapolation to avoid instrumental background and absorption from other edges [31]. The resulting element-resolved absorption μ(E) was afterwards normalized by using atomic-like absorption profiles. Careful fits to the measured data were carried out using the Artemis program included in the IFEFFIT software package. The fitted data for the first single scattering path included photoelectron waves with wave numbers of 3–10.5 Å^{-1} and interatomic distances of 1–3 Å for each element (Cr, Mn, Fe, Co, Ni).

First-principles calculations were carried out in the framework of density functional theory (DFT) with the VASP code [32,33] employing the projector-augmented wave (PAW) method [34] within the generalized gradient approximation (GGA) in the Perdew–Burke–Ernzerhof (PBE) parametrization [35]. The provided PAW potentials [36] with 3*d* and 4*s* electrons in the valence were employed. The planewave cutoff was set to 350 eV. Chemical disorder was simulated utilizing the concept of special quasi-random structures (SQS) [37]. The SQS approach enables an efficient simulation of chemical disorder within a (limited) supercell through optimizing the atomic distribution by minimizing the pair correlation functions. For a recent application of the SQS technique to high

entropy alloys, we refer to [38]. The supercell size for the SQS is usually chosen under three conditions: it should (a) resemble chemical disorder as good as possible, (b) match the experimental composition and (c) should be computationally efficient (i.e., not too large). An artificial ordering could impact total energies, as well as bond lengths. We, therefore, used a 125 atom SQS ($5 \times 5 \times 5$ primitive cells) minimizing the nearest and next-nearest neighbor pair correlation functions. Permutation of the five components results in 25 distinguishable SQS realizations for the chosen supercell. We have checked 5 such different permutations, and the results showed almost degenerate energies, as well as very similar bond lengths. This simulation result indicates that the chosen supercell provides a good representation of the random solid solution at reasonable computational efficiency. Each 125 atom supercell consisted of 25 atoms for each species, ideally resembling the equi-atomic composition. A $4 \times 4 \times 4$ Γ-centered k-point mesh and the Methfessel–Paxton method (order 1) with a smearing parameter of 0.1 eV were chosen for the Brillouin zone sampling. To study the impact of lattice expansion, all calculations were performed at 6 different lattice constants around the theoretical equilibrium. Magnetism was taken into account, and according to previous studies [11,13], a ferrimagnetic structure was initialized with Cr and Mn spins being aligned anti-parallel to the Fe, Co and Ni atomic spins.

Despite recent progress in describing vibrations in magnetic materials for pure elements and selected ordered magnetic alloys from DFT [39–42], these methods are not yet advanced to a stage being applicable to the present magnetic multi-component alloy and are therefore neglected in the present work. In order to elucidate the impact of magnetism, all calculations were additionally performed within non-spin polarized DFT.

3. Results and Discussion

The concept of computing element-specific lattice distortions is illustrated in Figure 2. From the different SQS supercell realizations, we extracted 1500 individual element-specific bonds for each of the five constituents. We considered an undistorted, ideal FCC lattice as the reference structure to quantify the experimentally-, as well as the theoretically-extracted bond length variations. As an example, Figure 2a indicates a few of the bonds for Mn for a specific SQS supercell, and Figure 2b shows the local bond variation of Mn averaged over all 1500 different bonds. In order to quantify the mean value, as well as the fluctuations (standard deviations), we performed Gaussian fits over the element-resolved data (the black line in Figure 2b). A direct outcome of the theoretical analysis is the comparably small mean distortion (<1%) compared to the fluctuation (standard deviation) of the individual bond lengths, which can be in the order of a few percent.

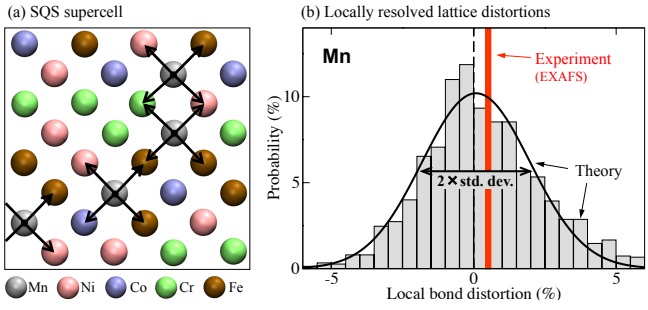

Figure 2. (**a**) Projection of one of the employed special quasi-random structure (SQS) supercells onto the (100) plane. The black arrows indicate the nearest neighbor bonds for the Mn atoms that are used to extract the distribution of the local bond distortions as shown in (**b**). In (**b**), the first-principles computed lattice distortion histogram of Mn-bonds in FeCoNiCrMn is based on 1500 evaluated Mn-bonds. The theoretical data are further analyzed by Gaussian fits (see the text for details). The experimentally-measured averaged distortion is indicated by the red solid line. Although the mean distortion is rather small (<0.5%), the range of local distortions at the standard deviation is significant (≈2%), as indicated in (**b**).

The same analysis has been carried out for all individual elements. The bond distortion distributions are shown in Figure 3a–e, revealing the strongest variation for Cr and Mn. In Figure 3f–o, we also show the mean values of the bond distributions and the corresponding standard deviations versus mean bond length. This allows us to reveal the impact of volumetric changes, which could arise from temperature or pressure variations. The theoretical mean values in Figure 3f–j derived from the Gaussian fits (open black circles), as well as the standard mean values (filled black circles) agree well with the experimentally obtained EXAFS data (red open squares). The largest fluctuation in the theoretical (Figure 3k–o) and experimental data (red error bars in Figure 3f–j) is consistently found for Cr and Mn. Note that the overall magnitude of the local bond fluctuations quantified by the standard deviations in Figure 3k–o is almost an order of magnitude larger than the corresponding mean averaged distortions. They are also much larger than the actual deviation between theory and experiment for the mean averaged distortions. For example, the largest deviation between theory and experiment is found for the mean bond distortions of Mn (shown in Figure 3j). However, comparing in Figure 2b the peak of the Gaussian fit (black solid line) and the EXAFS data (red dashed line) with the fluctuations indicated by the standard deviation relativizes the seemingly large deviation of the mean values. Note that at room temperature, harmonic thermal excitations (phonons), which are not considered in our current theoretical framework, can further broaden the resulting bond length distribution, but will not significantly affect the derived mean bond lengths which are compared to the experiment. Further analyzing the theoretical volume-dependent data shown in Figure 3f–o reveals that the mean distortions are rather robust with respect to changes in volume. However, this is in contrast to the standard deviations revealing a strong volume dependence. This indicates a sensitive interplay between temperature or pressure induced volume changes and local bond fluctuations. Overall a good agreement between the theoretical and experimental data is found.

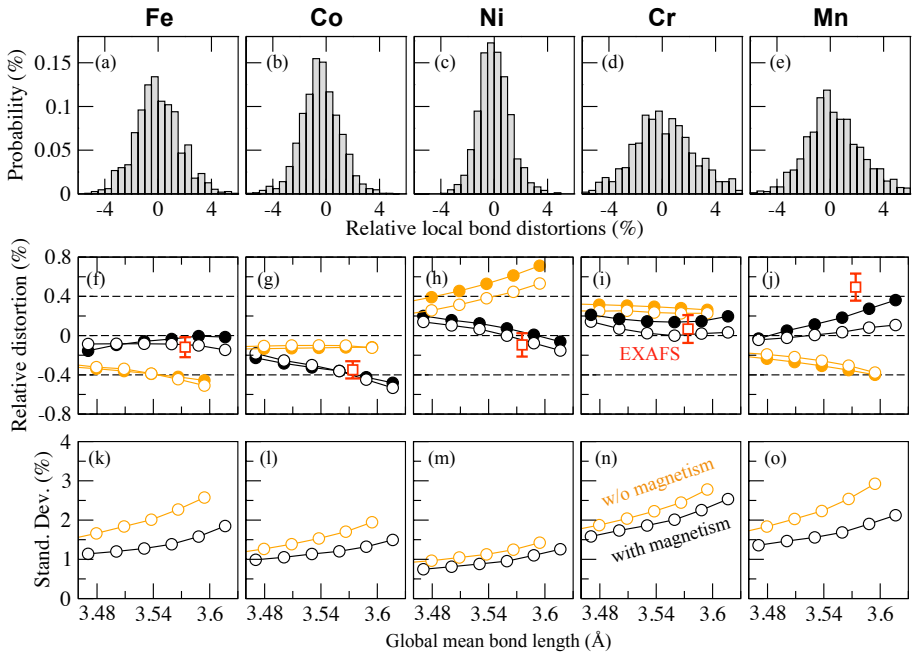

Figure 3. (**a**–**e**) Pair-resolved distribution of relative local bond distortions for Fe, Co, Ni, Cr and Mn determined from first-principles calculations of in total 3750 individual atomic bonds. The standard deviations of the bond distribution are an order of magnitude larger than the actual mean displacement. (**f**–**j**) Experimental EXAFS data (red open squares) compared to the theoretical mean bond length (black filled circles), as well as the mean value derived from a Gaussian fit (black open circles) for different volumes. Non-spin polarized calculations are shown for comparison (open and filled orange circles). (**k**–**o**) Standard deviation of the Gaussian fits revealing the much larger local bond distortions compared to actual mean, averaged values.

In all cases, the standard deviation of the local bond lengths σ_b is about an order of magnitude greater than the mean difference between the local bond length and the global average bond length $\Delta\overline{b}$. This observation has great implications for the solute strengthening mechanism in HEAs. A full derivation of the solute strengthening model in systems with fluctuating misfit volumes is beyond the scope of this work, but the relative importance of the σ_b can be seen by examining how it affects the fluctuation in solute-dislocation interaction energy. This term is closely related to Labusch-type strengthening [14,15].

When the local bond length (and hence, the local misfit) is small, the bond length is proportional to the misfit volume,

$$\frac{\Delta V^i}{\overline{V}} = \frac{8\pi K}{\sqrt{2}} \frac{\Delta b^i}{b_\circ}, \tag{3}$$

where $K = 3(1-\nu)/(1+\nu)$ is the Eshelby constant, ν is Poisson's ratio and Δb^i is the relative distortion of a solute of type i [43].

In this case, the interaction energy between a dislocation at the origin and a solute can be expressed as:

$$U^i(\vec{r}) = p(\vec{r})\, K\overline{V} \left(\Delta\overline{b}^i + \delta b^i(\vec{r}_i) \right) / b_\circ, \tag{4}$$

where $\Delta\overline{b}^i$ is the mean difference between the bond length of solute i, the global mean bond length $b_\circ$, δb^i is the local fluctuating part of the bond length and $\overline{V}$ is the mean atomic volume of the alloy. The mean interaction energy is then:

$$\overline{U}^i(\vec{r}) = p(\vec{r})\, K\overline{V}\Delta\overline{b}^i / b_\circ, \tag{5}$$

and the standard deviation of the interaction energy is:

$$\sigma_U^i(\vec{r}) = p(\vec{r})\, K\overline{V}\sigma_b^i / b_\circ. \tag{6}$$

From Figure 3, it is clear that $\overline{U}^i \ll \sigma_U^i$. That is, for HEAs, the fluctuation of the local bond length (and hence, the local misfit volume) cannot be ignored.

As mentioned above, the strongest fluctuations in local bonds have been identified for Cr and Mn. As both are anti-ferromagnetic elements in contrast to the other three ferromagnetic constituents Fe, Co and Ni, it stands to reason that magnetism is responsible for this effect. In order to estimate the impact of magnetism, we performed all of the calculations in the non-spin polarized formulation of DFT. The results for the mean values are shown in Figure 3f–o (orange circles). We find that the agreement between theory and experiment for the mean bond distortions, which we have found for the magnetic results, is completely lost when comparing to the non-magnetic calculations. Inspecting the results in more detail, we find that Ni, the element with the smallest atomic radius, reveals the largest mean bonds in the alloy. This shows that non-spin polarized simulations are clearly not sufficient to describe the properties of the real alloy. Interestingly, the fluctuations of all constituents are increased if magnetism is switched off. In this case, even Fe reveals strong local bond fluctuations. The unique dominant role of Cr and Mn in for local bond fluctuations is, however, lost without taking magnetism into account. We can, therefore, conclude that magnetism is responsible for the unique character of local bond fluctuations in this alloy and is critically required for realistic simulations.

In order to further elucidate the important role of Cr and Mn, we show in Figure 4 the individually element-element resolved mean bond distortions and corresponding standard deviations. Consistent with our discussion above, the mean distortions are much smaller than the corresponding standard deviations. An important outcome of this analysis is that Cr and Mn not only induce strong local bond fluctuations among themselves, i.e., for Cr-Cr, Cr-Mn and Mn-Mn bonds, but also in combination with the other elements, e.g., for Cr-Fe and Mn-Fe. This indicates that alloying

multi-component alloys with Cr and Mn can induce serious local bond fluctuations, although the overall mean alloy distortions appear to be rather small. In fact, a strong relation between alloying with Cr and Mn and mechanical properties for different HEAs has been reported. The relation to local bond fluctuation will be discussed elsewhere.

Mean distortion (in %)

	Fe	Co	Ni	Cr	Mn
Fe	0.34	-0.72	-0.06	0.18	0.22
Co	-0.72	-0.43	-0.08	-0.67	-0.22
Ni	-0.06	-0.08	0.04	0.02	0.12
Cr	0.18	-0.67	0.02	0.66	0.54
Mn	0.22	-0.22	0.12	0.54	0.71

Standard deviation (in % of distortion)

	Fe	Co	Ni	Cr	Mn
Fe	1.58	1.21	1.15	2.09	1.99
Co	1.21	1.14	1.03	1.88	1.40
Ni	1.15	1.03	0.89	1.38	1.16
Cr	2.09	1.88	1.38	3.06	3.01
Mn	1.99	1.40	1.16	3.01	2.74

Figure 4. Element-resolved mean bond distortions and standard deviation in the fcc FeCoNiCrMn HEA. Cr and Mn induce strong local bond fluctuations for all considered elemental pairs.

4. Conclusions

Element-resolved local distortions have been investigated in fcc FeCoNiCrMn combining EXAFS measurements and electronic structure calculations. Good agreement between the experimental and theoretical data is found for the element-resolved mean lattice distortions. These turned out to be relatively small (∼0.1%), explaining the recent success of theoretical simulations assuming undistorted perfect lattices.

However, the local fluctuations of the lattice distortions are an order of magnitude larger than the mean and can significantly impact solute strengthening in these class of materials. Therefore, using results from mean field theories is not well suited to predict quantities that depend on the fluctuations in the local lattice distortions (such as the yield strength), since these methods cannot capture these local fluctuations, which can amount up to 2%–3%. The local bond fluctuations can impact dislocation-solute interaction energies and, hence, contribute to solid-solution strengthening much stronger than the actual mean bond distortions. These insights provide vital input for solid solution strengthening models in HEAs [16] and enable more physically-sound simulations of the distortions and dislocation mechanics in this new and promising class of alloys.

Acknowledgments: We thank Andrei V. Ruban for providing the spcm program for generating the special quasi-random structures. Funding by the scholarship KO 5080/1-1 of the Deutsche Forschungsgemeinschaft (DFG), the European Research Council (ERC) under the European Union's Horizon 2020 research and innovation program (Grant Agreement No. 639211), as well as by the National Research Foundation of Korea (NRF) under the Korean Government (Ministry of Science, ICT and Future Planning) (NRF-2014M1A7A1A01030139) is gratefully acknowledged.

Author Contributions: Hyun Seok Oh performed the experiments supervised by Eun Soo Park and Dierk Raabe. DFT calculations have been performed by Duancheng Ma and analyzed together with Fritz Körmann, Blazej Grabowski and Gerard Paul Leyson. All authors have equally contributed to the overall discussion and preparation of the manuscript, as well as read and approved the final manuscript version.

Conflicts of Interest: The authors declare no conflict of interest.

References

1. Murty, B.S.; Yeh, W.J.; Ranganathan, S. *High-Entropy Alloys*; Elsevier: London, UK, 2014.
2. Zhang, Y.; Zuo, T.T.; Tang, Z.; Gao, M.C.; Dahmen, K.A.; Liaw, P.K.; Lu, Z.P. Microstructures and properties of high-entropy alloys. *Prog. Mater. Sci.* **2014**, *61*, 1–93, doi:10.1016/j.pmatsci.2013.10.001.
3. Gao, M.; Yeh, J.; Liaw, P.; Zhang, Y. *High-Entropy Alloys: Fundamentals and Applications*; Springer: Cham, Switzerland, 2016.
4. Gludovatz, B.; Hohenwarter, A.; Catoor, D.; Chang, E.H.; George, E.P.; Ritchie, R.O. A fracture-resistant high-entropy alloy for cryogenic applications. *Science* **2014**, *345*, 1153–1158.
5. Zou, Y.; Ma, H.; Spolenak, R. Ultrastrong ductile and stable high-entropy alloys at small scales. *Nat. Commun.* **2015**, *6*, doi:10.1038/ncomms8748.

6. Li, Z.; Pradeep, K.G.; Deng, Y.; Raabe, D.; Tasan, C.C. Metastable high-entropy dual-phase alloys overcome the strength–ductility trade-off. *Nature* **2016**, *534*, 227–230.
7. Yao, M.; Pradeep, K.; Tasan, C.; Raabe, D. A novel, single phase, non-equiatomic FeMnNiCoCr high-entropy alloy with exceptional phase stability and tensile ductility. *Scr. Mater.* **2014**, *72*, 5–8.
8. Deng, Y.; Tasan, C.C.; Pradeep, K.G.; Springer, H.; Kostka, A.; Raabe, D. Design of a twinning-induced plasticity high entropy alloy. *Acta Mater.* **2015**, *94*, 124–133.
9. Zhang, Y.; Zuo, T.; Cheng, Y.; Liaw, P.K. High-entropy alloys with high saturation magnetization, electrical resistivity, and malleability. *Sci. Rep.* **2013**, *3*, doi:10.1038/srep01455.
10. Jin, K.; Sales, B.C.; Stocks, G.M.; Samolyuk, G.D.; Daene, M.; Weber, W.J.; Zhang, Y.; Bei, H. Tailoring the physical properties of Ni-based single-phase equiatomic alloys by modifying the chemical complexity. *Sci. Rep.* **2016**, *6*, doi:10.1038/srep20159.
11. Körmann, F.; Ma, D.; Belyea, D.D.; Lucas, M.S.; Miller, C.W.; Grabowski, B.; Sluiter, M.H. "Treasure maps" for magnetic high-entropy-alloys from theory and experiment. *Appl. Phys. Lett.* **2015**, *107*, 142404.
12. Huang, S.; Vida, Á.; Molnár, D.; Kádas, K.; Varga, L.K.; Holmström, E.; Vitos, L. Phase stability and magnetic behavior of FeCrCoNiGe high-entropy alloy. *Appl. Phys. Lett.* **2015**, *107*, 251906.
13. Ma, D.; Grabowski, B.; Körmann, F.; Neugebauer, J.; Raabe, D. Ab initio thermodynamics of the CoCrFeMnNi high entropy alloy: Importance of entropy contributions beyond the configurational one. *Acta Mater.* **2015**, *100*, 90–97.
14. Labusch, R. A statistical theory of solid solution hardening. *Phys. Status Solidi* **1970**, *41*, 659–669.
15. Labusch, R. Statistical theories of solid solution hardening (Concentration of solute atoms, interaction range between solute atoms and distortion, and interaction strength of solid solution hardening). *Acta Metall.* **1972**, *20*, 917–927.
16. Varvenne, C.; Luque, A.; Curtin, W.A. Theory of strengthening in fcc high entropy alloys. *Acta Mater.* **2016**, *118*, 164–176.
17. Fleischer, R. Solution hardening. *Acta Metall.* **1961**, *9*, 996–1000.
18. Wang, S. Atomic Structure Modeling of Multi-Principal-Element Alloys by the Principle of Maximum Entropy. *Entropy* **2013**, *15*, 5536–5548.
19. Egami, T.; Ojha, M.; Khorgolkhuu, O.; Nicholson, D.; Stocks, G. Local electronic effects and irradiation resistance in high-entropy alloys. *JOM* **2015**, *67*, 2345–2349.
20. Niu, C.; Zaddach, A.; Oni, A.; Sang, X.; Hurt, J., III; LeBeau, J.M.; Koch, C.C.; Irving, D.L. Spin-driven ordering of Cr in the equiatomic high entropy alloy NiFeCrCo. *Appl. Phys. Lett.* **2015**, *106*, 161906.
21. Tamm, A.; Aabloo, A.; Klintenberg, M.; Stocks, M.; Caro, A. Atomic-scale properties of Ni-based FCC ternary, and quaternary alloys. *Acta Mater.* **2015**, *99*, 307–312.
22. Troparevsky, M.C.; Morris, J.R.; Daene, M.; Wang, Y.; Lupini, A.R.; Stocks, G.M. Beyond Atomic Sizes and Hume-Rothery Rules: Understanding and Predicting High-Entropy Alloys. *JOM* **2015**, *67*, 2350–2363.
23. Li, X.; Tian, F.; Schönecker, S.; Zhao, J.; Vitos, L. Ab initio-predicted micro-mechanical performance of refractory high-entropy alloys. *Sci. Rep.* **2015**, *5*, doi:10.1038/srep12334.
24. Huang, S.; Li, W.; Lu, S.; Tian, F.; Shen, J.; Holmström, E.; Vitos, L. Temperature dependent stacking fault energy of FeCrCoNiMn high entropy alloy. *Scr. Mater.* **2015**, *108*, 44–47.
25. Tian, F.; Delczeg, L.; Chen, N.; Varga, L.K.; Shen, J.; Vitos, L. Structural stability of NiCoFeCrAl x high-entropy alloy from ab initio theory. *Phys. Rev. B* **2013**, *88*, 085128.
26. Körmann, F.; Ruban, A.V.; Sluiter, M.H. Long-ranged interactions in bcc NbMoTaW high-entropy alloys. *Mater. Res. Lett.* **2016**, doi:10.1080/21663831.2016.1198837.
27. Yeh, J.W.; Chang, S.Y.; Hong, Y.D.; Chen, S.K.; Lin, S.J. Anomalous decrease in X-ray diffraction intensities of Cu–Ni–Al–Co–Cr–Fe–Si alloy systems with multi-principal elements. *Mater. Chem. Phys.* **2007**, *103*, 41–46.
28. Guo, W.; Dmowski, W.; Noh, J.Y.; Rack, P.; Liaw, P.K.; Egami, T. Local atomic structure of a high-entropy alloy: An X-ray and neutron scattering study. *Metall. Mater. Trans. A* **2013**, *44*, 1994–1997.
29. Otto, F.; Dlouhỳ, A.; Pradeep, K.; Kuběnová, M.; Raabe, D.; Eggeler, G.; George, E. Decomposition of the single-phase high-entropy alloy CrMnFeCoNi after prolonged anneals at intermediate temperatures. *Acta Mater.* **2016**, *112*, 40–52.
30. Newville, M. IFEFFIT: Interactive XAFS analysis and FEFF fitting. *J. Synchrotron Radiat.* **2001**, *8*, 322–324.
31. Newville, M. Fundamentals of XAFS. *Rev. Mineral. Geochem.* **2014**, *78*, 33–74.

32. Kresse, G.; Furthmüller, J. Efficient iterative schemes for ab initio total-energy calculations using a plane-wave basis set. *Phys. Rev. B* **1996**, *54*, 11169.
33. Kresse, G.; Furthmüller, J. Efficiency of ab-initio total energy calculations for metals and semiconductors using a plane-wave basis set. *Comput. Mater. Sci.* **1996**, *6*, 15–50.
34. Blöchl, P.E. Projector augmented-wave method. *Phys. Rev. B* **1994**, *50*, 17953.
35. Perdew, J.P.; Burke, K.; Ernzerhof, M. Generalized gradient approximation made simple. *Phys. Rev. Lett.* **1996**, *77*, 3865.
36. Kresse, G.; Joubert, D. From ultrasoft pseudopotentials to the projector augmented-wave method. *Phys. Rev. B* **1999**, *59*, 1758.
37. Zunger, A.; Wei, S.H.; Ferreira, L.; Bernard, J.E. Special quasirandom structures. *Phys. Rev. Lett.* **1990**, *65*, 353.
38. Gao, M.C.; Niu, C.; Jiang, C.; Irving, D.L. Applications of Special Quasi-random Structures to High-Entropy Alloys. In *High-Entropy Alloys: Fundamentals and Applications*; Springer: Cham, Switzerland, 2016; pp. 333–368.
39. Körmann, F.; Grabowski, B.; Dutta, B.; Hickel, T.; Mauger, L.; Fultz, B.; Neugebauer, J. Temperature Dependent Magnon-Phonon Coupling in bcc Fe from Theory and Experiment. *Phys. Rev. Lett.* **2014**, *113*, 165503.
40. Körmann, F.; Hickel, T.; Neugebauer, J. Influence of magnetic excitations on the phase stability of metals and steels. *Curr. Opin. Solid. St. Mater.* **2016**, *20*, 77–84.
41. Körmann, F.; Ma, P.W.; Dudarev, S.L.; Neugebauer, J. Impact of magnetic fluctuations on lattice excitations in fcc nickel. *J. Phys. Condens. Matter* **2016**, *28*, 076002.
42. Alling, B.; Körmann, F.; Grabowski, B.; Glensk, A.; Abrikosov, I.; Neugebauer, J. Strong impact of lattice vibrations on electronic and magnetic properties of paramagnetic Fe revealed by disordered local moments molecular dynamics. *Phys. Rev. B* **2016**, *93*, 224411.
43. Uesugi, T.; Higashi, K. First-principles studies on lattice constants and local lattice distortions in solid solution aluminum alloys. *Comput. Mater. Sci.* **2013**, *67*, 1–10, doi:10.1016/j.commatsci.2012.08.037.